

# Flow Sensing for Height Estimation and Control of a Rotor in Ground Effect: Modeling and Experimental Results

**Chin Gian Hooi**

chingian.hooi@umd.edu

**Francis D. Lagor**

flagor@umd.edu

**Derek A. Paley**

dpaley@umd.edu

Graduate Research Assistant   Graduate Research Assistant   Willis H. Young Jr. Associate Professor

*Department of Aerospace Engineering and Institute for Systems Research  
University of Maryland, College Park, MD, USA*

## ABSTRACT

This paper describes a dynamic controller for rotorcraft landing and hovering in ground effect using feedback control based on flowfield estimation. The rotor downwash in ground effect is represented using a ring-source potential flow model selected for real-time use. Experimental verification of the flow model is also presented. A nonlinear dynamic model of the rotorcraft in ground effect is presented with open-loop analysis and closed-loop control simulation. Experimental results of the open-loop dynamics are presented and the effect of motor dynamics on the overall dynamics are investigated. Flowfield velocity measurements are assimilated into a grid-based recursive Bayesian filter to estimate height above ground in both simulation and experiment. Height tracking in ground effect and landing are implemented with a dynamic linear controller. Experimental validation of the closed-loop controller is ongoing.

## INTRODUCTION

Rotorcraft operation in ground effect (IGE) presents substantial challenges for vehicle control, including landing with low-impact velocity and maintaining near-ground hover in low-visibility conditions such as brownout (Ref. 1), fog (Ref. 2), snow or darkness. Safe operation IGE requires a controller capable of handling uncertainty. Previous authors have developed landing controllers based on robust or adaptive control techniques. For example, Serra and Cunha (Ref. 3) adopt an affine parameter-dependent model that describes the helicopter linearized error dynamics for a predefined landing region and implements  $H_2$  feedback control. Mahony and Hamel (Ref. 4) develop a parametric adaptive controller that estimates the helicopter aerodynamics onboard and modulates the motor torque, rather than the collective pitch, during take-off and landing and takes advantage of the reduced sensitivity of the control input to aerodynamics effects. Nonaka and Sugizaki (Ref. 5) implement ground-effect compensation and integral sliding mode control to suppress the modeling error of the vehicle dynamics in ground effect. These control techniques often require a system model with empirically fit aerodynamic coefficients that are unique to each vehicle.

Safe operation IGE also requires accurate estimation of the proximity and relative orientation of the ground plane. Height-estimation methods currently exist for micro aerial vehicles (MAVs) based on ultrasonic, barometric pressure or optical sensors. However, ultrasonic sensors work only for proximity sensing and do not work well for an angled or irregular ground plane (Ref. 6). Barometric pressure sensors typically

work well for large height differentials (Ref. 7), but are sensitive to fluctuations in atmospheric pressure, which results in sensor drift. Likewise, the effectiveness of vision-based sensors is limited in degraded visual environments. This paper develops a hover and landing controller that uses rotor downwash flow-velocity measurements and an aerodynamic model to estimate the height above ground, thereby providing an additional sensing modality for hovering and landing IGE.

Previous authors have quantified ground effect empirically or through the use of an underlying aerodynamic model. Nonaka and Sugizaki (Ref. 5) take an empirical approach to measuring the ground effect on rotor thrust as a function of motor voltage. Mahony and Hamel (Ref. 4) use an approximation of the down-flow velocity ratio based on a piecewise linear approximation of Prouty (Ref. 8) to estimate rotor-thrust variation IGE. Higher fidelity analytical models include prescribed wake vortex modeling (Ref. 9) and free vortex modeling (Ref. 10), which seek to accurately predict the nature of the rotor wake vortices. Cheeseman and Bennett (Ref. 11) provide a classic analytical model for ground effect, which we adopt for this work, based on aerodynamic modeling using the method of images. The use of an aerodynamic model permits comparison to measurements from sensors such as multi-component differential-pressure airspeed sensors (Ref. 12). Lagor et al. (Ref. 13) and DeVries et al. (Ref. 14) have previously shown that a reduced-order flow model can be rapidly evaluated within a Bayesian filter to perform estimation and control tasks in an uncertain flow environment.

Our previous paper (Ref. 15) developed a dynamic controller for hover and landing IGE based on a flow model for height estimation. Rotorcraft downwash IGE was modeled using potential flow theory. We extended the model of Cheeseman and Bennett (Ref. 11) using multiple ring sources;

---

Presented at the AHS 71st Annual Forum, Virginia Beach, Virginia, May 5–7, 2015. Copyright © 2015 by the American Helicopter Society International, Inc. All rights reserved.

the mirror images create a ground plane. The reduced-order model relates the flowfield velocities to height IGE; it is capable of relatively fast evaluation for control purposes. A nonlinear dynamic model of rotorcraft landing IGE was presented, assuming a rigid rotor commonly found in MAV rotorcraft (Ref. 16). Height estimation of rotorcraft IGE using spatially distributed airspeed measurements was accomplished with a grid-based recursive Bayesian filter. The Bayesian framework is capable of fusing data from additional sensing modalities and for estimation of additional states, such as roll and pitch relative to the landing platform. The feedback controller was implemented in simulation to illustrate the theoretical results.

This paper expands on our previous paper by including experimental verification of parts of the flow modeling, sensing and control framework. The contributions of this paper are (1) an improved ring-source potential flow model consistent with experimental observations; (2) a nonlinear dynamics model of a compound pendulum heave test stand; (3) experimental verification of our ring-source potential flow model and height estimation framework; and (4) experimental results of the open-loop compound pendulum dynamics.

## Flow Estimation and Closed-Loop Control System Architecture

The control and estimation architecture developed and simulated in this paper is shown in Fig. 1. The flow velocities  $v$  and  $w$ , in the radial and vertical axes, respectively, are simulated using the ring-source potential flow model. The rotorcraft dynamics are simulated using a nonlinear state-space model. Flow measurements  $\tilde{v}$  and  $\tilde{w}$  are presumed to be corrupted with additive sensor noise. These flow measurements are used by a grid-based recursive Bayesian filter to estimate rotorcraft height and a feedback controller seeks to drive the vehicle to the commanded height.

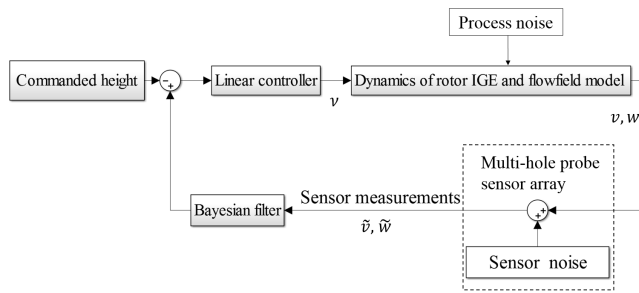


**Fig. 1. Block diagram for closed-loop flow sensing and control.**

## Experimental Instrumentation Architecture

Experiments described in this paper were conducted to verify and implement the theoretical framework presented above. Fig. 2 shows a block diagram of the experimental instrumentation, which is categorized into three parts: sensing (blue), estimation and control (green), and actuation (purple). The

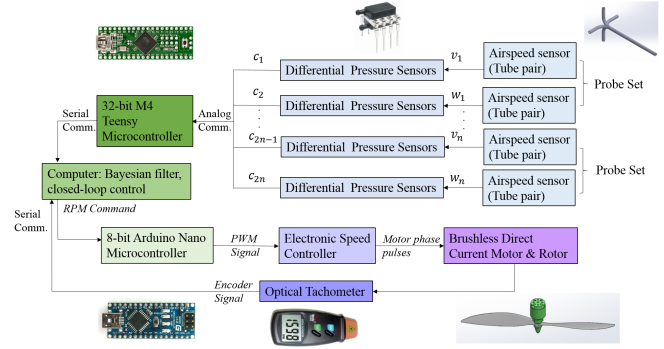


**Fig. 2. Block diagram for experimental instrumentation.**

airspeed probe sets are connected to differential pressure sensors to measure radial and vertical flow pressure. The pressure measurements are collected by a Teensy microcontroller for filtering and conversion into velocity components. These velocity measurements are transmitted to the computer for height estimation and closed-loop control. Finally, the Arduino Nano microcontroller actuates the brushless direct circuit motor and rotor pair, and the motor speed is measured by an optical tachometer and transmitted back to the computer.

## FLOW MODEL

### Cheeseman and Bennett Flow Model IGE

Let  $R$  be the rotor radius,  $v_i$  denote the rotor induced velocity and  $h$  be the rotor height. Cheeseman and Bennett (Ref. 11) model the rotor downwash impinging on the ground plane by representing the rotor as a three-dimensional source with strength  $s = R^2 v_i / 4$  and the ground plane as a mirror-image source to enforce no flow through the ground plane, as shown in Fig. 3. The sources are separated by a distance  $2h$ .

The velocity potential for the location  $(x, y, z)$  in the flowfield is (Ref. 11)

$$\phi = -\frac{s}{\sqrt{x^2 + y^2 + (z-h)^2}} - \frac{s}{\sqrt{x^2 + y^2 + (z+h)^2}}. \quad (1)$$

Taking the gradient of the velocity potential with respect to position yields the flow velocity components (Ref. 11).

Although the Cheeseman and Bennett flow model has been experimentally shown to accurately capture the relationship between rotor thrust IGE and rotor height (Ref. 11), it represents the physical flowfield of a rotor IGE with insufficient accuracy for our purposes. As shown in Fig. 3, the flow vectors just below the rotor plane extend radially outward as opposed to downward. Since the rotor is modeled as a point source, the strongest vectors are at the hub and diffuse in strength radially outward.

### Ring-Source Potential Flow Model

Similar to the Cheeseman and Bennett model, we model the physical flowfield using potential flow theory. However, we replace the single source of Cheeseman and Bennett radially

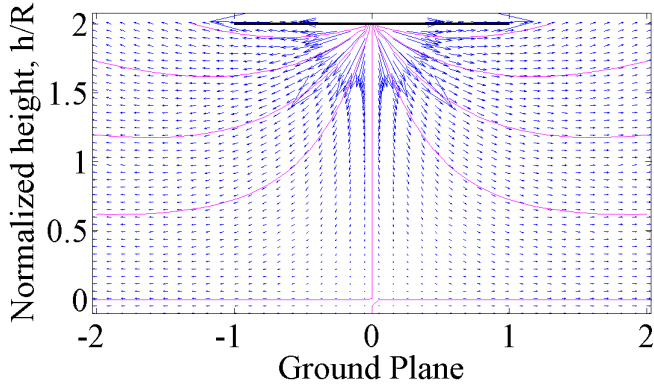


**Fig. 3. Cheeseman and Bennett [11] potential flow model of rotor downwash in ground effect.**

outward into ring sources to create a more uniform spatial distribution of the flowfield sources.

As shown in Fig. 4, the rotor is modeled by ring sources and the ground plane is modelled by their mirror image to enforce no flow through the ground plane. Note that ring  $k = 1$  is at the rotor tip and the ring indices move radially inward with equal radial spacing of  $R/N$ . The radial location of each ring  $k$  is

$$r_k = R - (k-1) \frac{R}{N}. \quad (2)$$

Similar to the inflow ratio distribution of a rotor (Ref. 17), the strength  $s_k$  of ring  $k$  varies with radial location according to

$$s_k = \frac{s_{max}}{R} r_k, \quad (3)$$

where the maximum source strength  $s_{max}$  is located at the rotor tip  $r_1 = R$ . We choose the source strengths according to the total volumetric flow through the rotor disk, similar to Cheeseman and Bennett. Let  $A = \pi R^2$  denote the rotor disk area. The strength of each ring source  $s_k$  represents the volumetric flow rate per unit length and the total flow rate satisfies

$$\frac{1}{2} \sum_{k=1}^N 2\pi r_k s_k - \frac{1}{4} (2\pi R s_{max}) = Av_i. \quad (4)$$

Although the ring sources emanate in all directions, only the bottom half of the emanation should be modeled as the rotor flow. Additionally, the outer most ring source, which happens to be the strongest, should only have a quarter of its emanation considered because the emanation outwards and upwards do not contribute to the rotor flow. Substituting (2) and (3) into (4) and using arithmetic series along with the sum of a sequence of squares yields

$$s_{max} = \frac{6NRv_i}{2N^2 + 1}. \quad (5)$$

The velocity potential of ring source  $k$  is (Ref. 18)

$$\phi_k(r, r_k, z) = \frac{-s_k r_k K(M)}{\pi \sqrt{\rho_1(r, r_k, z)}}, \quad (6)$$

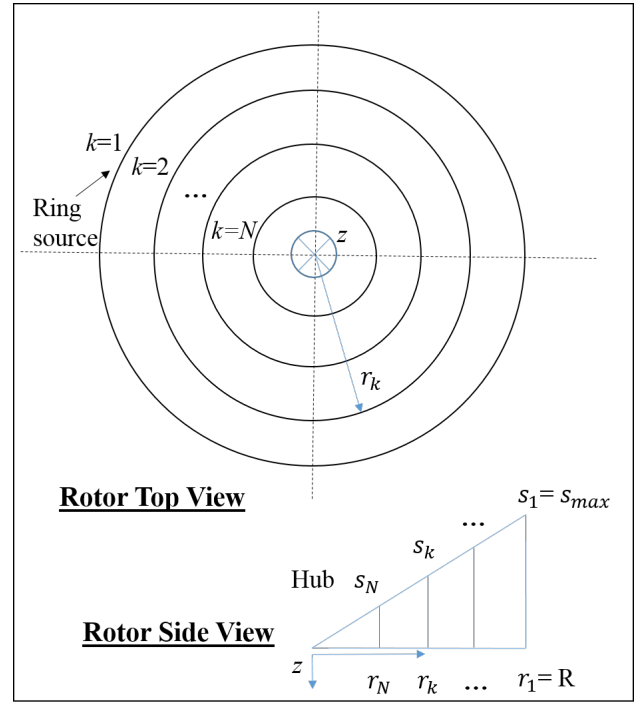


**Fig. 4. Schematic of ring-source potential flow model nomenclature.**

where  $\rho_1 = (r + r_k)^2 + z^2$ ,  $r$  and  $z$  are the radial location and elevation of the query point in the rotor body frame (positive down), respectively, and  $M = 4rr_k/\rho_1$ . Note that the radial  $v_k(\rho_1, \rho_2)$  and vertical  $w_k(\rho_1, \rho_2)$  velocity components of ring source  $k$  are (Ref. 18)

$$v_k = \frac{r_k s_k}{2\pi r \sqrt{\rho_1}} \left[ K(M) + \frac{r^2 - r_k^2 - z^2}{\rho_2} E(M) \right] \quad (7)$$

$$\text{and } w_k = \frac{s_k r_k - z E(M)}{\pi \rho_2 \sqrt{\rho_1}}, \quad (8)$$

where  $\rho_2 = (r - r_k)^2 + z^2$  and  $K(M)$  and  $E(M)$  are the first and second complete elliptic integrals respectively. ( $K(M)$  and  $E(M)$  are evaluated using the `elliptic` function in MATLAB<sup>®</sup>.) The velocity components of the flowfield are the sum of each ring source and their image ring-source contributions, i.e.,

$$v(r, z) = \sum_{k=1}^N v_k(\rho_1, \rho_2) + \sum_{k=1}^N v_k(\bar{\rho}_1, \bar{\rho}_2), \quad (9)$$

$$w(r, z) = \sum_{k=1}^N w_k(\rho_1, \rho_2) + \sum_{k=1}^N w_k(\bar{\rho}_1, \bar{\rho}_2), \quad (10)$$

where  $\bar{\rho}_1 = (r + r_k)^2 + (2h - z)^2$  and  $\bar{\rho}_2 = (r - r_k)^2 + (2h - z)^2$ .

Fig. 5 shows the flowfield generated by the ring-source potential flow model, with streamlines and speed distribution shown for various heights. Speed is denoted by  $\|V\| = \sqrt{v^2 + w^2}$ . The variations in speed distribution with height serve as an informative tool for the placement of sensors to measure the flowfield experimentally. The potential flow

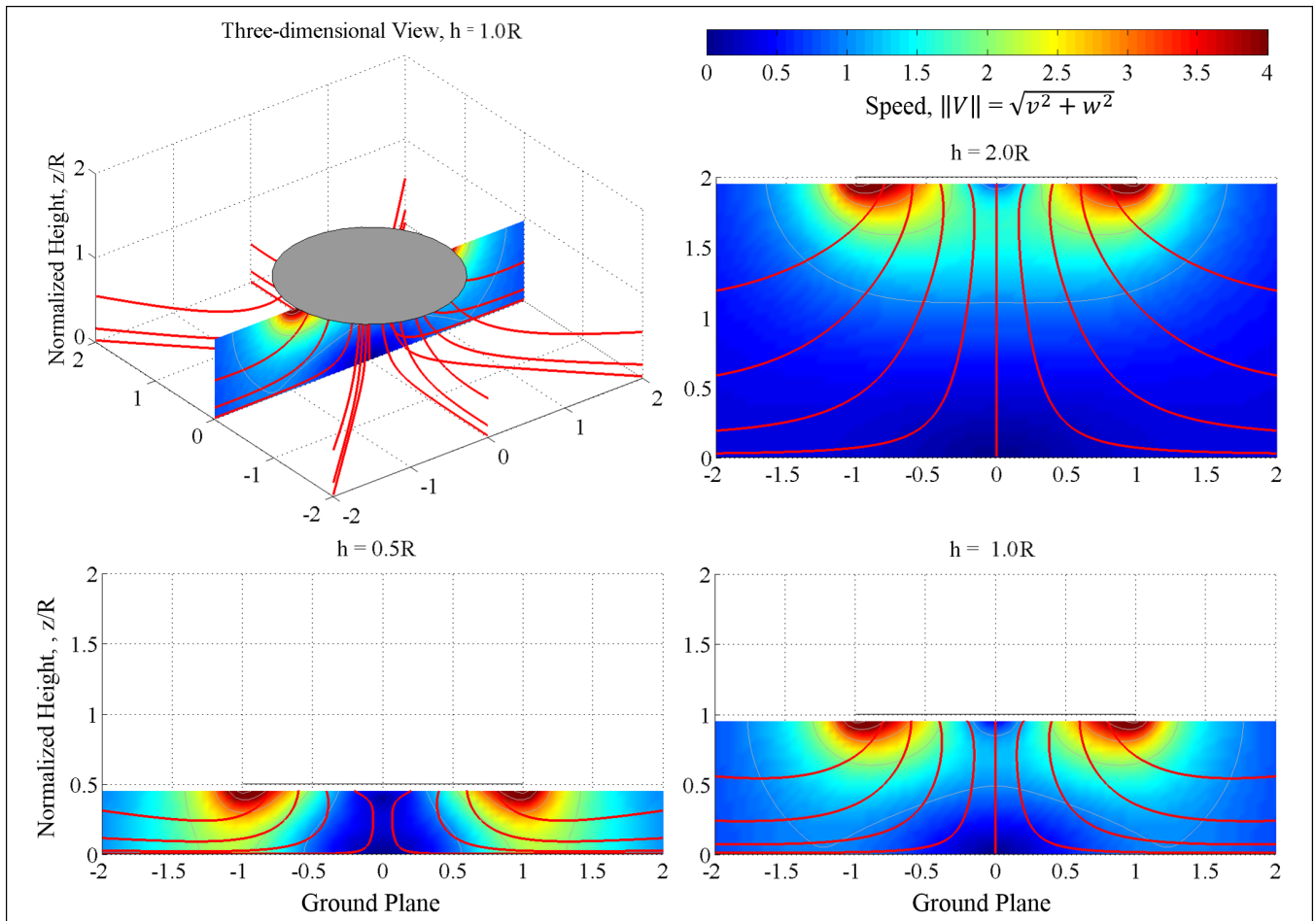


**Fig. 5. Flowfield of ring-source potential flow model evaluated at various heights, depicting streamlines and speed distributions, where speed  $\|V\| = \sqrt{v^2 + w^2}$ .**

model is qualitatively similar to the flow visualization model of the flow below a rotor IGE by Lee et al. (Ref. 19).

Moving from the rotor plane to the ground close to the rotor hub, the flow decelerates and forms a stagnation region. The flow deceleration region is easiest to distinguish for  $h=1.0R$  in Fig. 5. In contrast, the flow acceleration region is where the streamlines change direction from pointing downward to pointing radially outward. As the rotor approaches the ground, the streamlines are compressed, which is best illustrated for  $h=0.5R$  in Fig. 5. Evidently, the flow speed is the highest in the flow acceleration region for the  $h=0.5R$  case as opposed to the  $h=2.0R$  case, since the flow is being compressed more with less space between the rotor plane and the ground. This effect is analogous to moving a water jet (the rotor) closer to a wall (the ground plane), since the jet speed in the flow acceleration region is highest when it is close to the wall.

Although the rotor downwash IGE as visualized in the work of Lee et al. (Ref. 19) is not laminar, we model it using potential flow theory and account for turbulence with process noise (see Height and Speed Estimation Section). We model the mean velocity of the dominant flow and treat the

turbulence and other secondary effects, such as blade tip vortices, as fluctuations away from the mean. Flow velocity component measurements  $\tilde{V}$  are collected below the rotor in the experimental setup. Airspeed measurements of the sort described in (Ref. 12) contain two flow velocity components, radial  $\tilde{v}$  and vertical  $\tilde{w}$ , at each airspeed probe set location and are collected in an array configuration to sample the flowfield at multiple spatial locations. Measurement  $\tilde{V}$  corresponds to either the radial  $\tilde{v}$  or the vertical  $\tilde{w}$  velocity component. We assume  $\tilde{V}$  is corrupted by zero-mean Gaussian white noise  $\eta$  with standard deviation  $\sigma_\eta$  and zero mean, resulting in the measurement model

$$\tilde{V} = V + \eta. \quad (11)$$

## DYNAMICS AND CONTROL

### Dynamics of Rotorcraft Operation IGE

Fig. 6 shows the free-body diagram of a rotorcraft in which the tailrotor counter torque is not shown. Applying Newton's second law in the  $e_z$  direction yields

$$m\ddot{h} = T_{IGE} - mg - b_1\dot{h}, \quad (12)$$

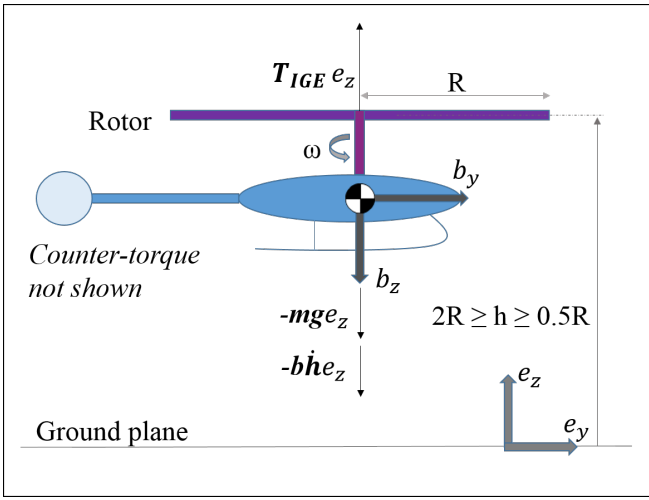


**Fig. 6. Free-body diagram of rotorcraft in ground effect.**

where  $T_{IGE}$  is the rotor thrust IGE,  $m$  is the mass of the rotor,  $\dot{h}$  and  $\ddot{h}$  are the vertical velocity and acceleration respectively,  $g$  is the gravitational acceleration and  $b_1$  is the damping coefficient due to aerodynamics or another source. Modeling the rotor thrust  $T$  as a function of rotor rotational speed  $\omega$  yields (Ref. 16)

$$T = k\omega^2. \quad (13)$$

The rotor thrust is augmented for ground effect using the Cheeseman and Bennett model, which captures the essential characteristic of the relationship between thrust and height IGE, i.e.,

$$T_{IGE} = \frac{1}{1 - \frac{R^2}{16h^2}} T = \frac{16h^2}{16h^2 - R^2} T. \quad (14)$$

Based on experimental data, Leishman (Ref. 17) suggests that model (14) is valid for  $2.0 \geq h/R \geq 0.5$ . It is assumed henceforth that the rotorcraft has landed when  $h/R = 0.5$ , which is reasonable since the rotor distance above the landing gear is typically greater than  $0.5R$ . Thrust IGE (14) is substituted into (12) to obtain the dynamics of a rotorcraft IGE,

$$\ddot{h} = \frac{16h^2 k \omega^2}{(16h^2 - R^2)m} - g - b_1 \dot{h}. \quad (15)$$

### Linear State Space Form

The state vector  $Z \in \mathbb{R}^2$  is defined as

$$Z = \begin{bmatrix} h \\ \dot{h} \end{bmatrix} = \begin{bmatrix} z_1 \\ z_2 \end{bmatrix}, \quad (16)$$

where  $\dot{h}$  is the landing speed. Since the rotor rotational speed is unregulated, we define  $v = k\omega^2/m$  as the control input. The nonlinear state space form is

$$\dot{Z} = \begin{bmatrix} \dot{h} \\ \ddot{h} \end{bmatrix} = \begin{bmatrix} z_2 \\ \frac{16z_1^2}{16z_1^2 - R^2} v - g \end{bmatrix}. \quad (17)$$

An equilibrium control input  $v^*$  is necessary to keep the rotorcraft hovering at a corresponding equilibrium height  $z_1^*$  (or to land safely). Solving (17) for the equilibrium condition,  $\dot{Z} = 0$ , the equilibrium control input is

$$v^* = g \frac{16z_1^{*2} - R^2}{16z_1^{*2}}. \quad (18)$$

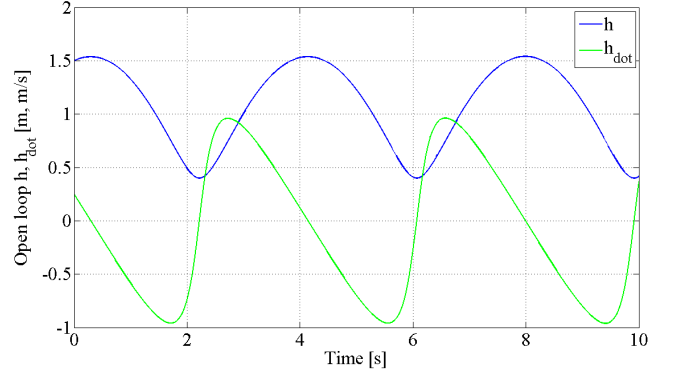


**Fig. 7. Open-loop dynamics of rotorcraft in ground effect with constant input  $v = v^*$ . Initial conditions for height and speed are (1.5m, 0.25m/s).**

Fig. 7 depicts the simulation results of the open-loop nonlinear dynamics for initial height and speed (1.5m and 0.25m/s) and constant input  $v = v^*$ .

In order to implement a linear controller for the nonlinear dynamics (17), the Jacobian matrices are needed. The Jacobians

$$A = \begin{bmatrix} 0 & 1 \\ \frac{-2gR^2}{z_1^*(16z_1^{*2} - R^2)} & 0 \end{bmatrix} \quad \text{and} \quad B = \begin{bmatrix} 0 \\ \frac{16z_1^{*2}}{16z_1^{*2} - R^2} \end{bmatrix} \quad (19)$$

are the partial derivatives of the right-hand side of (17) with respect to  $Z$  and  $v$ , respectively. The linear system dynamics are

$$\dot{Z} = AZ + Bv. \quad (20)$$

### Nonlinear Dynamics with Linear Observer-based Feedback Control

The state space system (17) in control affine form is

$$\dot{Z} = f(Z) + g(Z)v, \quad (21)$$

where

$$f(Z) = \begin{bmatrix} z_2 \\ -g \end{bmatrix} \quad \text{and} \quad g(Z) = \begin{bmatrix} 0 \\ \frac{16z_1^2}{16z_1^2 - R^2} \end{bmatrix}. \quad (22)$$

Fig. 7 shows that the constant-input open-loop nonlinear system with  $v = v^*$  oscillates about the equilibrium point, which implies that feedback control is needed to asymptotically stabilize  $z_1$  to the desired height. A linear controller to be used with the nonlinear system dynamics is

$$v = v^* + \Delta v, \quad (23)$$

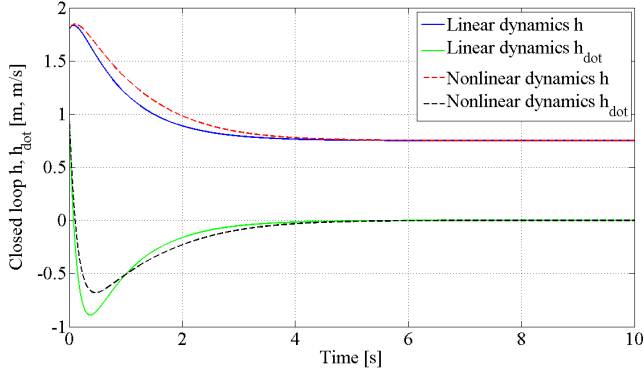


**Fig. 8. Closed-loop dynamics of rotorcraft in ground effect with full-state feedback,  $\hat{Z} = Z$  using the linear controller (23).**

where  $\Delta v = -K(\hat{Z} - Z^*)$ ,  $K = [K_1 \ K_2]$  and  $\hat{Z} = [\hat{z}_1 \ \hat{z}_2]^T$  denotes the estimated states. The closed-loop dynamics with the linear output-feedback controller (23) are

$$\dot{Z} = \begin{bmatrix} z_2 \\ -g \end{bmatrix} + \begin{bmatrix} 0 \\ \frac{16z_1^2}{16z_1^2 - R^2} \end{bmatrix} (v^* + \Delta v), \quad (24)$$

i.e.,

$$\dot{Z} = \begin{bmatrix} z_2 \\ -g + \frac{16z_1^2}{16z_1^2 - R^2} \left( g \frac{16z_1^2 - R^2}{16z_1^2} - K_1(\hat{z}_1 - z_1^*) - K_2\hat{z}_2 \right) \end{bmatrix}. \quad (25)$$

Figure 8 compares the nonlinear closed-loop dynamics (25) to the linear closed-loop dynamics (20), using linear controller (23). The simulation is implemented using full-state feedback,  $\hat{Z} = Z$ . The optimal gains  $K$  are provided by Linear Quadratic Regulator (LQR) and the Jacobian matrices in (19) are evaluated at the equilibrium height. Initial conditions for the height and speed are (1.8m, 0.9m/s) and desired steady-state conditions are (0.75m, 0m/s).

### Dynamics of Compound Pendulum Heave Test Stand

Our experimental setup was constructed as a compound pendulum with one degree of freedom in the heave direction as shown in Fig. 9. This setup allows the use of journal bearings, which are smoother than linear carriages and rails in a vertical setup. This setup also has the added benefit of allowing a counterweight to balance the system weight and to reduce the motor load. Figure 10 shows the free-body diagram of the compound pendulum. The lateral ( $e_y$ ) displacement can be minimized by mounting the setup at the midstroke, i.e., at a height of  $1.25R$ .

The angular momentum of the compound pendulum is

$$h_o = I_o \dot{\theta} e_x, \quad (26)$$

where  $I_o$  is the moment of inertia about point  $O$ ,  $\theta$  is the positive clockwise angle from vertical and  $\dot{\theta}$  is the angular velocity of the pendulum. The time derivative of the angular momentum equals the moment about point  $O$ . In the  $e_x$  direction,

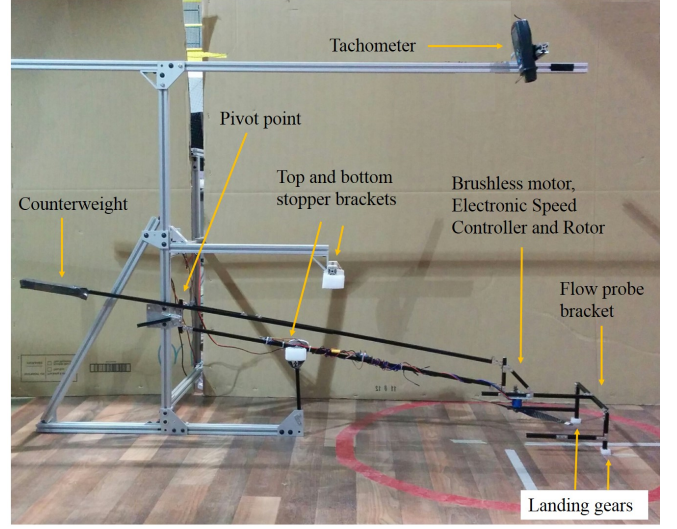


**Fig. 9. Compound pendulum heave test stand.**

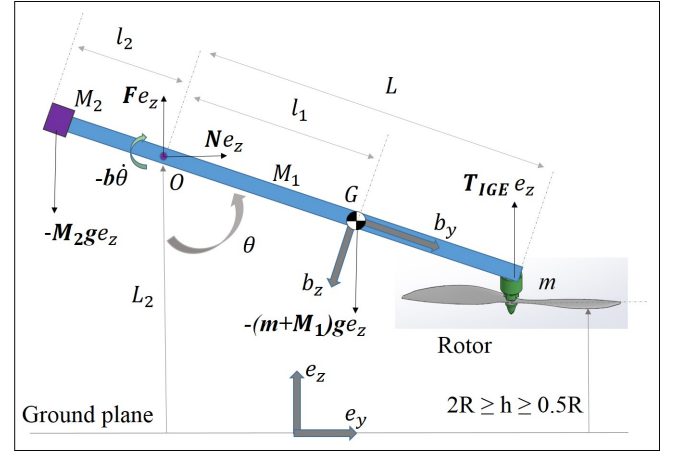


**Fig. 10. Free body diagram of compound pendulum heave test stand.**

we have

$$I_o \ddot{\theta} = L T_{IGE} \sin \theta - l_1 g \sin \theta (m + M_1) + l_2 M_2 g \sin \theta - b_2 \dot{\theta}, \quad (27)$$

where  $\ddot{\theta}$  is the angular acceleration;  $l_1$ ,  $l_2$  and  $L$  are the distances from  $O$  to the center of mass,  $O$  to counterweight  $M_2$  and  $O$  to rotor mass  $m$  respectively;  $M_1$  is the mass of the pendulum setup and  $b_2$  is the damping coefficient due to aerodynamics and/or friction. In terms of the height  $h = L_2 - L \cos \theta$ , we have

$$\dot{h} = L \dot{\theta} \sin \theta, \quad (28)$$

$$\ddot{h} = L \dot{\theta}^2 \cos \theta + L \ddot{\theta} \sin \theta. \quad (29)$$

Since the compound pendulum is mounted at midstroke, we approximate  $\theta \approx \pi/2$ , which implies

$$h \approx L_2, \quad \dot{h} \approx L \dot{\theta} \quad \text{and} \quad \ddot{h} \approx L \ddot{\theta}. \quad (30)$$

Likewise, the moment of inertia  $I_o$  is

$$I_o = mL^2 + \frac{1}{3} M_1 (L + l_2)^2 + M_2 l_2^2. \quad (31)$$

Substituting (14) and (30) into (27) yields the dynamics of the compound pendulum heave test stand,

$$\ddot{h} = \frac{1}{I_o} \left[ \frac{16h^2 k \omega^2 L^2}{(16h^2 - R^2)} - l_1 L g (m + M_1) + l_2 L g M_2 \right] - b \dot{h}, \quad (32)$$

where  $b = b_2/I_o$ . Note that as the mass of the compound pendulum setup  $M_1$  and the counterweight  $M_2$  go to zero, the compound pendulum dynamics (32) reduce to the rotorcraft IGE dynamics (15).

## HEIGHT AND SPEED ESTIMATION

The Bayesian filter (Ref. 14) (Ref. 20) is a probabilistic approach for estimation that assimilates noisy measurements into a probability density function (PDF) using nonlinear system dynamics and observation operators. (The optimal Bayesian filter for linear systems with linear measurements and Gaussian noise is the Kalman filter (Ref. 21), whereas a common Bayesian filter for nonlinear systems with nonlinear observation and noise models is the particle filter (Ref. 22).) A grid-based recursive Bayesian filter can be rapidly implemented for a low-dimensional state-space representation of the rotorcraft downwash with linear parameter estimates and a nonlinear measurement model.<sup>1</sup> It is of note that even though linear parameter estimates and Gaussian white noise is assumed for our measurement and process noise, these are not required assumptions for the Bayesian filter.

### Estimation Step

The Bayesian framework consists of the estimation and the prediction step. In the estimation step, the Bayesian filter in the form of (Ref. 14) estimates the vehicle height based on the flow-velocity measurements from an array of differential pressure sensors. Grid-based Bayesian estimation is performed recursively, in which the finite parameter space over height  $h$  is discretized and the PDFs are evaluated on this grid for each new measurement. Let  $h$  be the single state of a one-dimensional Bayesian filter. Recall that the noisy flow measurement  $\tilde{V}$  is corrupted with zero mean Gaussian noise as in (11). Let  $L = \{\tilde{V}_1, \dots, \tilde{V}_m\}$  denote the set of observations from  $m$  sensors. Note that each velocity component measurement (even at the same location) is treated as a separate measurement. The posterior probability of the state  $h$  given the measurements  $L$  is (Ref. 14)

$$P(h|L) = c P(L|h) P(h|L_0), \quad (33)$$

where  $c$  is the scaling factor chosen so that  $P(h|L)$  has unit integral over the state space. The likelihood function  $P(L|h)$

<sup>1</sup>As an alternative, the Unscented Kalman filter (Ref. 23) is an approximate nonlinear estimator that differs the inevitable divergence with highly nonlinear systems or measurements (Ref. 21). The particle filter (Ref. 22) provides high performance estimation but requires careful selection of its estimation state vector because it is prone to sample impoverishment and requires careful tuning.

is the conditional probability of the observations  $L$  given the state  $h$  and  $P(h|L_0)$  represents the prior probability distribution. During initialization or in the absence of measurements, the prior probability  $P(h|L_0)$  is uniform.

We choose a Gaussian likelihood function for the measurements  $\tilde{V}_l, l = 1, \dots, m$ , i.e.,

$$P(\tilde{V}_l|h) = \frac{1}{\sqrt{2\pi}\sigma} \exp \left[ -\frac{1}{2\sigma^2} (\tilde{V}_l - V_l)^2 \right], \quad (34)$$

where  $V_l$  is the flow at height  $h$  generated from the flow model (9) or (10) and  $\sigma^2$  is the measurement variance. The posterior probability density of the state  $h$  is obtained using the joint measurement likelihood combining the measurements taken from all  $m$  sensors (Ref. 14), i.e.,

$$P(h|L) = c \left( \prod_{l=1}^m P(\tilde{V}_l|h) \right) P(h|L_0). \quad (35)$$

The estimated height  $\hat{h}$  corresponding to the mode (supremum) of the posterior probability  $P(h|L)$  provides the maximum likelihood estimate of the flowfield parameters.

Spatial integration over the sensor array is accomplished by (35), whereas temporal integration is accomplished by assigning the posterior of the current time step to be the prior for the next time step.

### Prediction Step

The prediction step consists of shifting and diffusing the probability mass to account for the vehicle dynamics using the Chapman-Kolmogorov equation (Ref. 22),

$$P(h(t + \Delta t)|L(t)) = \int P(h(t + \Delta t)|h(t)) P(h(t)|L(t)) dh(t), \quad (36)$$

where  $t$  is the current time step and  $\Delta t$  is the time step interval. Numerically, the probability density is shifted along the grid according to the estimated speed  $\hat{z}_2$ . If the estimated speed  $\hat{z}_2$  is positive, we shift the PDF to the right and vice-versa. The number of grid points to shift is determined by the product of the estimated speed  $\hat{z}_2$  and time interval. After shifting, the probability density is normalized to ensure the PDF integrates to one.

To account for uncertainty in the motion model, the probability density is diffused with process noise  $\gamma$  by convolution with a grid-sized Gaussian window whose width is inversely proportional to the standard deviation of the process noise  $\sigma_\gamma$ . (This step is done with the MATLAB<sup>®</sup> functions `gausswin` and `convn`.)

### Simulation Examples

Fig. 11 shows the evolution of the marginal probability density of estimated height during closed-loop ascent (Fig. 11(a)) and descent (Fig. 11(b)). Fig. 11(a) shows an ascent maneuver from initial normalized height and speed (with respect to

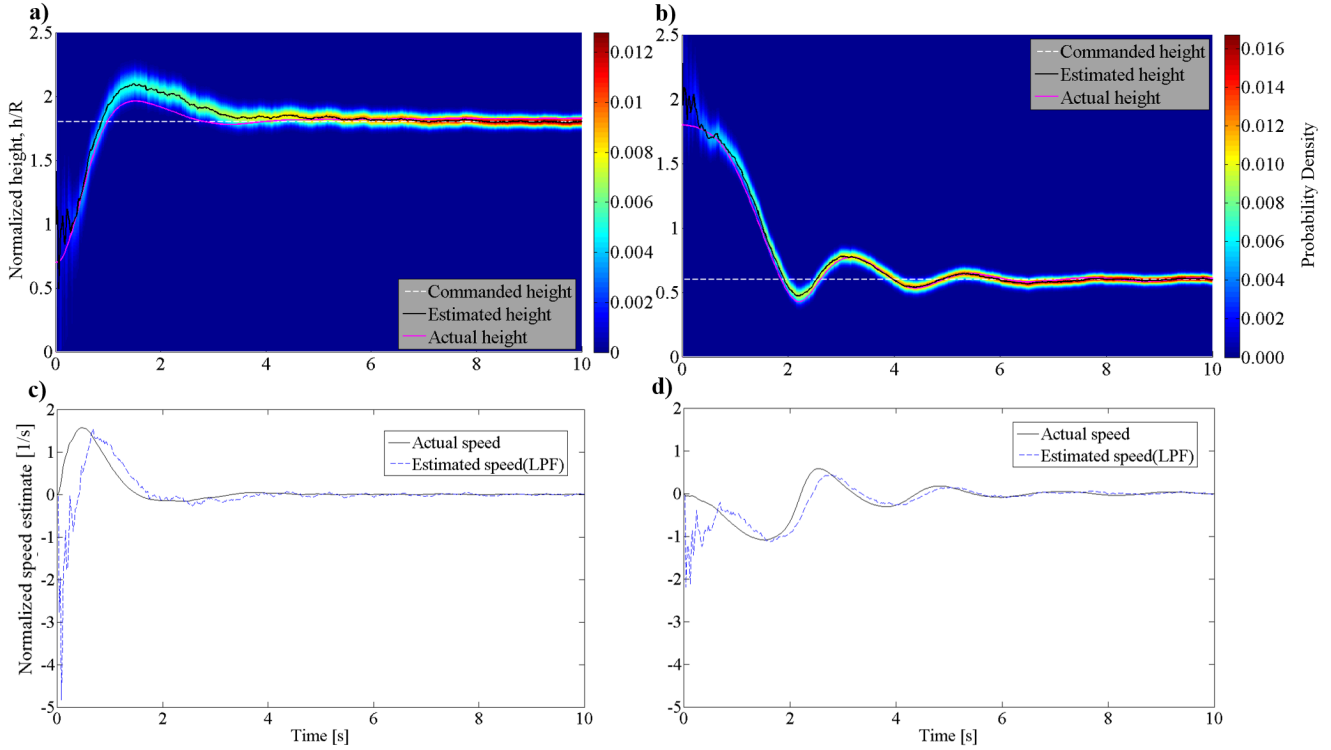


**Fig. 11. Simulations of the closed-loop control system with estimated height using the Bayesian filter framework show the marginal probability density of normalized height  $h/R$  and normalized speed plotted versus time. (a) Ascent maneuver from initial height and speed of (0.7, 0/s), commanded height of 1.8 and process and measurement noise standard deviation of (0.1, 0.15/s); (b) descent maneuver from initial height and speed of (1.8, 0.2/s), commanded height of 0.6 and process measurement noise standard deviation of (0.08, 0.1/s); (c) estimated speed using low-pass-filtered (LPF) finite differencing for ascent maneuver in (a); (d) estimated speed using low-pass-filtered (LPF) finite differencing for descent maneuver in (b).**

$R$ ) of (0.7, 0/s) to a commanded height of 1.8 and process and measurement noise standard deviation of (0.1, 0.15/s). Fig. 11(b) shows a descent maneuver from initial height and speed of (1.8, 0.2/s) to a commanded height of 0.6 and process and measurement noise standard deviation of (0.08, 0.1/s). Fig. 11(c) and (d) show the estimated speeds using the low-pass-filtered finite-differencing method (37) for ascent in (a) and descent in (b), respectively.

These maneuvers are simulated using the closed-loop dynamics (25). The estimated height  $\hat{z}_1$  is evaluated recursively by the one-dimensional Bayesian filter. The estimated height  $\hat{z}_2$  is evaluated from  $\hat{z}_1$  by finite differencing, i.e.,

$$\hat{z}_{2,p} = \alpha \hat{z}_{2,p-1} + (1 - \alpha) \frac{\hat{z}_{1,p} - \hat{z}_{1,p-1}}{\Delta t}, \quad (37)$$

where  $0 < \alpha < 1$ , the index  $p$  indicates the current time step and  $\Delta t$  is the time interval between each simulation step. Eq. (37) is a low-pass-filter that removes most of the effects of noise. Process noise  $\gamma$ , which is Gaussian white noise with standard deviation  $\sigma_\gamma$  and zero mean, is added to (25) in the filter.

Fig. 11(a) and (b) show that the initial height estimation error is large because the prior PDF is uniformly distributed.

As the Bayesian filter assimilates measurements over time, the marginal probability density peaks and the estimated height converges to the actual height. As more measurements are taken, the filter narrows the probability density. Note that Fig. 11(a) has a bigger spread throughout its probability density distribution than Fig. 11(b), due to the higher noise variances.

Fig. 11(c) and (d) show that the initial speed estimates are relatively large as the difference between successive height estimations is also relatively large. This effect is influenced by the Bayesian filter initiation and also the controller, which is driving the system to the commanded height. As the system reaches steady state at about 4s, the speed estimates begin to more closely track the actual speed. (The first-order speed estimation could be improved by using a higher-order estimation method.)

## EXPERIMENTAL RESULTS

Two heave test stands were built for experimental verification of the flow-sensing and control framework. Fig. 12 shows the static-height test stand to collect measurements of radial  $v$  and vertical  $w$  velocity components. The measurements are streamed in real time to a computer and compared to the ring-source models (9) and (10) to generate a static-height esti-

mate. Fig. 9 shows the compound pendulum heave test stand used to verify the dynamics and closed-loop control.

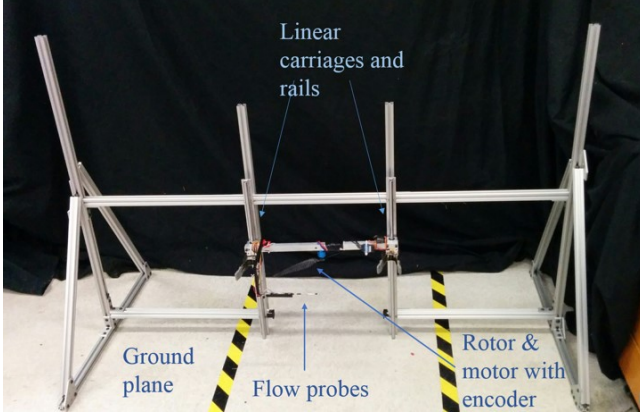


Fig. 12. Static-height test stand.

Table 1. Experimental Equipment.

Equipment	Model & Make
Brushless Direct Circuit Motor	850Kv AC2830-358
Differential Pressure Sensors	Honeywell HSCDRR001NDA A3
Direct Circuit Power Supply	Mastech HY3030E
Electronic Speed Controller	eRC Rapid Drive 25A
Modular Aluminum Profiles	MakerBeam & 8020
Microcontroller:	Cortex-M4 Teensy 3.1
Data Acquisition	
Microcontroller:	ATmega328
Motor Speed	Arduino Nano
Optical Tachometer	Neiko 20713A
Remote Control Radio	Spektrum DX6i
Rotor	HobbyKing 14X4.7
	Carbon Fiber
Scale	Ohaus Valor 100

Table 1 lists the make and model of the experimental equipment. Fig. 13 shows the instrumentation setup, which is common to both test stands. Note that the Remote Control (RC) radio is used for manual motor-speed control, whereas the Arduino Nano microcontroller is used for automatic speed control.

An airspeed probe set that is capable of measuring the radial and vertical velocity components consists of two pairs of tubes. Each pair is connected to a differential pressure sensor (Ref. 12). The pressure sensors are connected via an analog interface to the Teensy 3.1 Microcontroller for Data Acquisition (DAQ). Since the pressure measurements are relatively noisy and the pressure sensor and DAQ microcontroller are capable of higher data rates than the estimation and control loop in the computer, a Moving Average Filter (MAF) is implemented on the pressure measurements to generate velocity

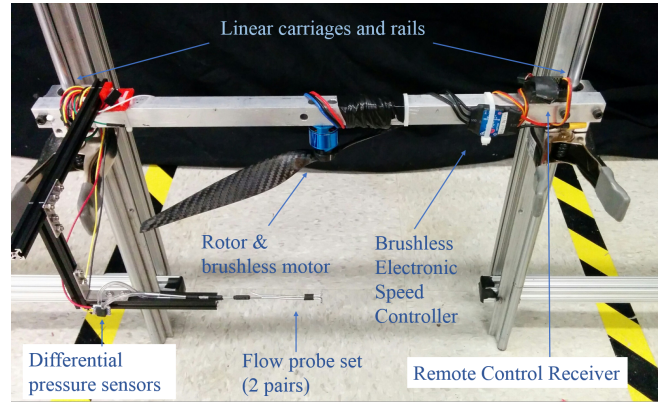


Fig. 13. Test stand instrumentation.

measurements  $\tilde{V}$ . The MAF implementation is

$$\tilde{V} = \frac{p}{J} \sum_{j=1}^J \tilde{P}_j, \quad (38)$$

where  $\tilde{P}_j$  is the instantaneous measurement from the differential pressure sensor,  $J$  is the number of datapoints to average over and  $p$  is the conversion factor from differential pressure to velocity (Ref. 12).

The actuation of the experimental setup consists of a Brushless Direct Circuit (BLDC) motor and Electronic Speed Controller (ESC) pair. Speed-control input requires Pulse Width Modulation (PWM) square wave signals with variable timescales, which are generated by the RC receiver or Arduino Nano microcontroller.

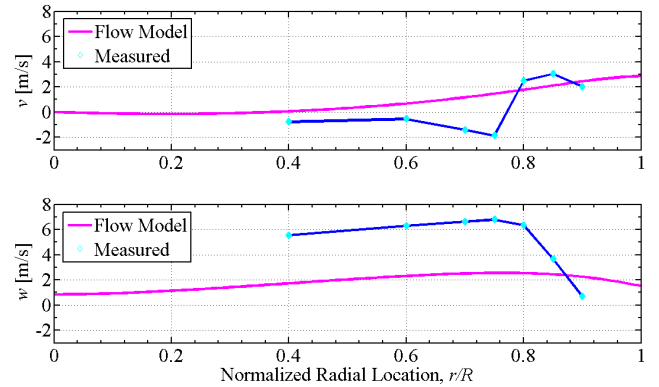
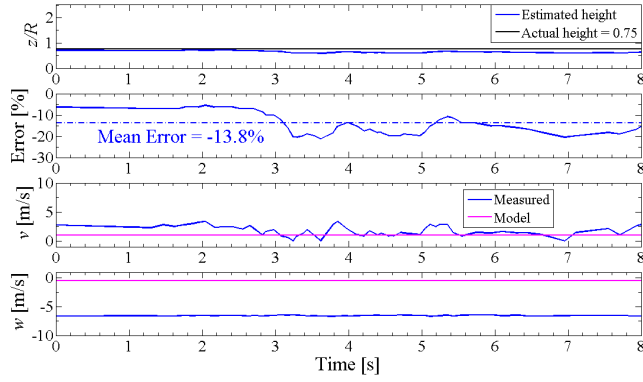


Fig. 14. Comparison between ring-source potential flow models (9), (10) and experimental results of radial  $v$  and vertical  $w$  velocity components for various radial locations. Normalized height  $z/R = 0.75$ , normalized sensor location  $(z/R)_{sensor} = 0.18$ , rotational speed  $\omega = 2538$  RPM, induced velocity IGE  $v_{i,IGE} = 4.34$  m/s.

#### Verification of Flow Model and Height Estimation Framework

Fig. 14 compares the measured radial and vertical velocity components with the flow model at normalized height  $z/R$



**Fig. 15.** Static height estimation at normalized height  $z/R=0.75$  for verification of ring-source potential flow models (9) and (10) using measured radial  $v$  and vertical  $w$  velocity components. Normalized sensor location  $(r/R, z/R)_{sensor} = (0.75, 0.18)$ , rotational speed  $\omega=2538$  RPM, induced velocity IGE  $v_{i,IGE} = 4.34$  m/s.

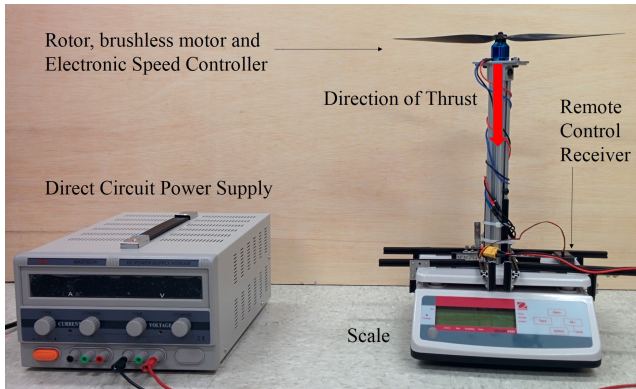


**Fig. 16.** Rotor Thrust Test Setup.

$= 0.75$ , with the sensors placed  $0.18R$  away from the rotor plane, motor rotational speed of 2538 RPM and induced velocity IGE  $v_{i,IGE}$  of 4.34 m/s. The induced velocity IGE is the average of vertical velocities close to the rotor plane across multiple radial locations and, in this case,  $z_{sensor}/R = 0.05$ .

The radial velocity crosses over from positive to negative at  $r/R=0.75$ , which represents suction toward the rotor hub. The model does not predict this outcome due to the geometry of the ring sources because inward flow at opposite sides of the same ring cancel out and radial velocity is always outward and positive. Furthermore, the radial flow is also influenced by turbulence and the tip vortices of each rotor blade, whereas the flow model captures only the mean velocity. The flow model underpredicts the vertical velocity component, which is likely because the induced velocity is an average rather than local value.

Fig. 15 shows the static height-estimation results at normalized height  $z/R = 0.75$  and normalized sensor locations at  $(r, z)_{sensor}/R = (0.75, 0.18)$ . The difference between the estimated height and the actual height has 13.8% mean error. Observed that the vertical velocity is relatively stable and the estimation errors are primarily caused by fluctuations in the

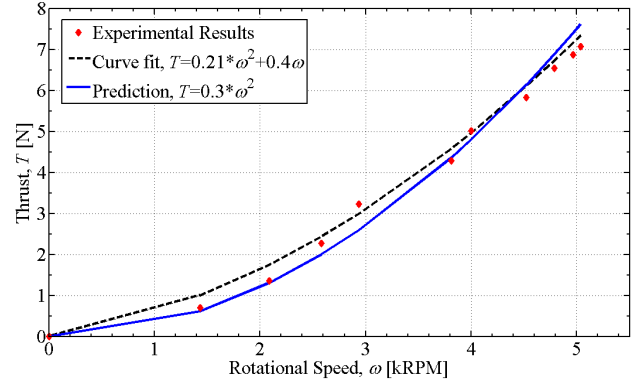


**Fig. 17.** Thrust  $T$  and rotational speed  $\omega$  relationship out of Ground Effect, comparing a curve fit and model (13) against experimental results.

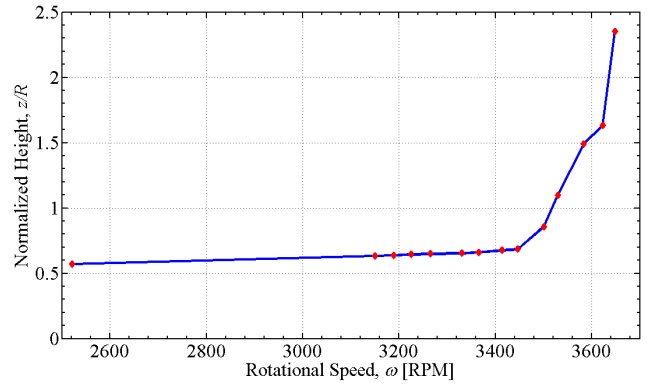


**Fig. 18.** Normalized height  $z/R$  and rotational speed  $\omega$  at steady-state in Ground Effect.

radial velocity.

### Open-Loop and Motor Dynamics

Fig. 16 shows the thrust test setup used to measure the relationship between rotor thrust  $T$  and rotational speed  $\omega$  OGE. The motor-ESC pair is mounted on the test stand, which is coupled with the scale. The DC Power Supply powers the motor-ESC pair and the Remote Control (RC) receiver controls the motor rotational speed. The rotor is mounted so that the thrust vector points downwards into the scale. This arrangement is primarily to facilitate operation OGE such that the ground does not impinge on the rotor downwash.

Fig. 17 shows the relationship between thrust and rotational speed OGE. The thrust model (13), including only second order terms ( $\omega^2$ ), is compared with experimental results and a curve-fit approach of both first and second order terms ( $\omega$  and  $\omega^2$ ). The thrust model fits the experimental results well on the lower rotational speeds and slightly overpredicts thrust on higher rotational speeds, whereas the curve-fit approach does the opposite. Since we are operating in the lower rotational speed regions around 3000–4000 RPM, as shown later in Fig. 18, the choice of the thrust model is justified. Note that ignoring the first order term also simplifies the dynamics (15).

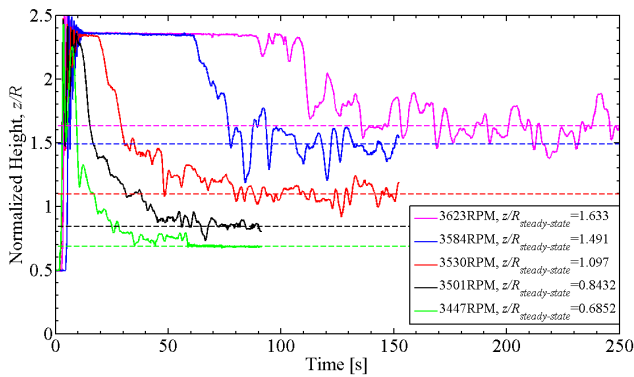


**Fig. 19. Normalized height  $z/R$  versus time in Ground Effect for various rotor rotational speeds starting from rest.**

Fig. 18 shows the steady-state open-loop dynamics of the compound-pendulum heave test stand by plotting the relationship between normalized height  $z/R$  and rotational speed  $\omega$  at steady-state. The height was measured by a Qualisys Motion Capture setup. The compound-pendulum heave test stand is at rest at  $z/R = 0.5$  and reaches its maximum height at  $z/R = 2.35$ . The plot depicts a highly nonlinear relationship with the height rising slowly at first up to 3447 RPM. From 3500 to 3865 RPM, each incremental increase in rotational speed results in a significant increase in height. The steep slope of this curve is a characteristic of the ESC-motor combination and a change of this combination could result in a more gradual response.

Fig. 19 shows the open-loop normalized height for various rotor rotational speeds starting from rest. There is a general trend of a steep increase in the height corresponding to the commanded input and the height decreases to the steady-state value. As the rotational speed increases, it takes longer before the motor-ESC pair converges to the steady-state height. The increased settling time as rotational speed increases is due to the large difference between commanded rotational speed and rest. A smaller rotational speed difference will decrease the settling time.

At lower rotational speeds, the dynamics seem to be overdamped. At higher rotational speeds, oscillations of the dynamics model (32) are evident. The delayed convergence to steady-state height and height oscillations suggest that the motor-ESC dynamics introduce a time constant  $\tau$ . The motor-ESC dynamics are modeled as (Ref. 24)

$$\tau \dot{\omega} + \omega = f_{mot}(u), \quad (39)$$

where  $\dot{\omega}$  is the rotational acceleration and  $f_{mot}$  is the nonlinear rotational speed response as a function of the PWM command input  $u$ . In ongoing work, the closed-loop controller combines (39) with the compound-pendulum test stand dynamics (32).

## CONCLUSIONS

This paper describes a dynamic controller for rotorcraft landing and hovering in ground effect. A ring-source flow model for the rotor downwash IGE developed using potential flow

theory captures the essential characteristics of the relationship between flow velocity and height. The reduced-order flow model used for fast evaluation of the flowfield in a recursive control loop has been experimentally validated. A nonlinear dynamic model of rotorcraft landing IGE allows for the study of the open-loop dynamics and facilitates the design of a closed-loop controller. Both the steady-state and transient open-loop dynamics of the compound-pendulum heave test setup are experimentally investigated; a model of the motor dynamics is proposed. The height of the rotorcraft IGE is experimentally estimated with a grid-based recursive Bayesian filter using the three-dimensional flow model, nonlinear dynamic model and differential pressure probe measurements. Finally, flow-estimation-based closed-loop control is implemented in simulation, demonstrating that height estimation and control is possible using only flow sensors. Experimental validation of the closed-loop system is ongoing.

## ACKNOWLEDGMENTS

The authors gratefully thank William Craig, Derrick Yeo, Daigo Shishika, and Nitin Sydney for valuable discussions and assistance. This work is supported by the University of Maryland Vertical Lift Rotorcraft Center of Excellence Army Grant No. W911W61120012.

## REFERENCES

- <sup>1</sup>Tritschler, J., "Contributions to the Characterization and Mitigation of Rotorcraft Brownout," Doctor of Philosophy Dissertation, Department of Aerospace Engineering, University of Maryland, 2012.
- <sup>2</sup>Plank, V.G., Spatola, A.A., Hicks, J.R., "Fog Modification by Use of Helicopters," Air Force Cambridge Research Laboratories, U.S. Army Atmospheric Sciences Laboratory, AFCRL-70-0593, Environmental Research Papers No. 335, ECOM-5339, October 28, 1970.
- <sup>3</sup>Serra, P., Cunha, R., Silvestre, C., "On the Design of Rotorcraft Landing Controllers," 16th Mediterranean Conference on Control and Automation Ajaccio, France, June 25-27, 2008.
- <sup>4</sup>Mahony, R., Hamel, T., "Adaptive Compensation of Aerodynamic Effects during Takeoff and Landing Manoeuvres for a Scale Model Autonomous Helicopter," *European Journal of Control*, (2001)0:1-15, 2001.
- <sup>5</sup>Nonaka, K., Sugizaki, H., "Integral Sliding Mode Altitude Control for a Small Model Helicopter with Ground Effect Compensation," American Control Conference, San Francisco, CA, June 29 - July 01, 2011.
- <sup>6</sup>Borenstein, J., Koren, Y., "Obstacle Avoidance with Ultrasonic Sensors," *IEEE Journal for Robotics and Automation*, Vol. 4, No. 2, April 1988.

- <sup>7</sup>Tanigawa, M., Luinge, H., Schipper, L., Slycke, P., "Drift-Free Dynamic Height Sensor using MEMS IMU Aided by MEMS Pressure Sensor," Proceedings of the 5th Workshop on Positioning, Navigation and Communication, 2008.
- <sup>8</sup>Prouty, R.W., *Helicopter Performance, Stability, and Control*, Krieger Publishing Company, Florida, 2002.
- <sup>9</sup>Gilad, M., Chopra, I., Rand, O., "Performance Evaluation of a Flexible Rotor in Extreme Ground Effect," 37th European Rotorcraft Forum, Milan, Italy, 2011.
- <sup>10</sup>Govindarajan, B., "Evaluation of Particle Clustering Algorithms in the Prediction of Brownout Dust Clouds," Master's Thesis, Department of Aerospace Engineering, University of Maryland, August 2011.
- <sup>11</sup>Cheeseman, I.C., Bennett, W.E., "The Effect of the Ground on a Helicopter Rotor in Forward Flight," Reports & Memoranda No. 3021, Ministry of Supply, Aeronautical Research Council Reports and Memoranda, September 1955.
- <sup>12</sup>Yeo, D. W., Sydney, N., Paley, D., Sofge, D., "Onboard Flow Sensing For Downwash Detection and Avoidance On Small Quadrotor Helicopters," AIAA Guidance, Navigation and Control Conference 2015, accepted for publication.
- <sup>13</sup>Lagor, F.D., DeVries, L.D., Waychoff, K., Paley, D.A., "Bio-inspired Flow Sensing and Control: Autonomous Rheotaxis Using Distributed Pressure Measurements," *Journal of Unmanned System Technology*, Nov 2013.
- <sup>14</sup>DeVries, L.D., Lagor, F.D., Lei, H., Tan, X., Paley, D.A., "Distributed Flow Estimation and Closed-Loop Control of an Underwater Vehicle with a Multi-Modal Artificial Lateral Line," *Bioinspiration & Biomimetics*, special issue on "Hybrid and Multi-modal Locomotion," accepted for publication.
- <sup>15</sup>Hooi, C.G., Lagor, F., Paley, D., "Flow Sensing, Estimation and Control for Rotorcraft in Ground Effect," IEEE Aerospace Conference, Big Sky, Montana, March 2015.
- <sup>16</sup>Hooi, C.G., "Design, Rapid Prototyping and Testing of a Ducted Fan Microscale Quadcopter," 70th American Helicopter Society Society Annual Forum & Technology Display, Montreal, Quebec, Canada, May 2014.
- <sup>17</sup>Leishman, J.G., *Principles of Helicopter Aerodynamics*, 2nd. Ed., p.258 - 260, Cambridge University Press, New York, 2006.
- <sup>18</sup>Hess, J.L., Smith, A.M.O., "Calculation of Potential Flow about Arbitrary Bodies," *Progress in Aerospace Sciences*, Volume 8, p. 3940, 1967.
- <sup>19</sup>Lee, T.E., Leishman, J.G., Ramasamy, M., "Fluid Dynamics of Interacting Blade Tip Vortices with a Ground Plane," *Journal of the American Helicopter Society* 55, 022005, 2010.
- <sup>20</sup>Murphy, K., *Machine Learning: A Probabilistic Perspective*, The MIT Press, Cambridge, Massachusetts, London, 2012.
- <sup>21</sup>Simon, D., *Optimal State Estimation: Kalman, H Infinity, and Nonlinear Approaches*, 1st. Ed., p.465-466, John Wiley & Sons, Inc., New Jersey, 2006.
- <sup>22</sup>Arulampalam, M.S., Maskell, S., Gordon, N., Clapp, T., "A Tutorial on Particle Filters for Online Nonlinear/Non-Gaussian Bayesian Tracking," *IEEE Transactions on Signal Processing*, Vol. 50, No. 2, February 2002.
- <sup>23</sup>Julier, S., Uhlmann, J., "Unscented Filtering and Nonlinear Estimation", *Proceedings of the IEEE*, Vol. 92, No. 3, March 2004.
- <sup>24</sup>Petru, E.S., "Intelligent Control and Cooperation for Mobile Robots," Doctor of Philosophy Dissertation, University of Texas at Arlington, December 2011.